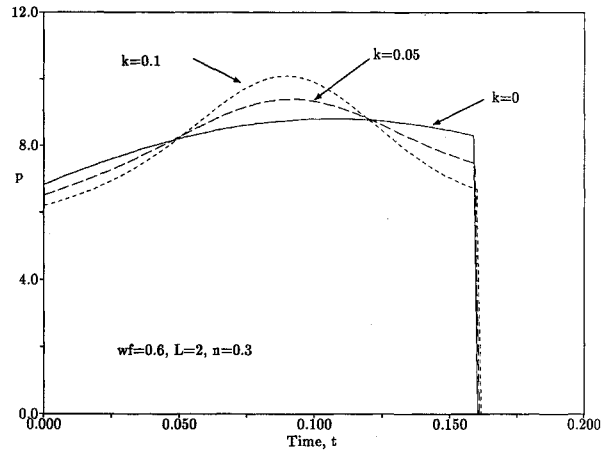

Fig. 3 Effect of spatial burning rate variations on chamber pressure.

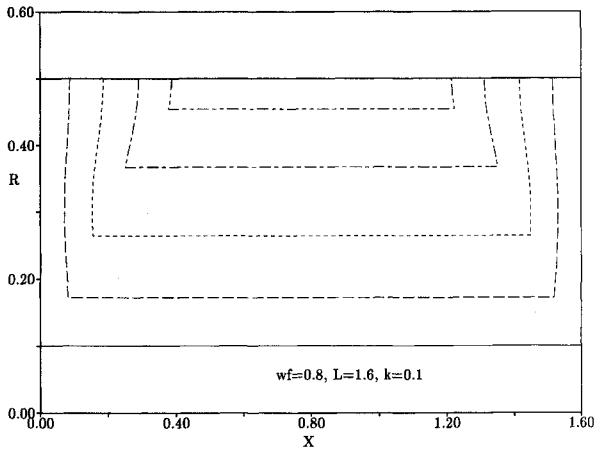

Fig. 4 Typical grain burnback pattern.

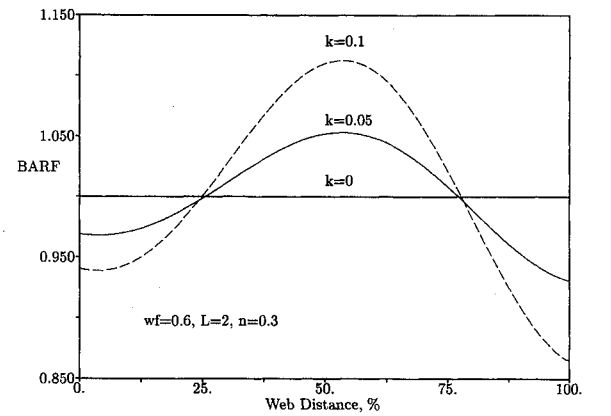

Fig. 5 Influence of spatial burning rate variation (factor k) on BARF curves.

curves can be generated by noting that BARF $\propto p^{(1-n)}$. Results of this calculation are shown in Fig. 5. This figure also indicates that moderate burning rate variations (e.g., only 1 or 2%) can lead to substantial BARF effects for a motor with a grain $L/D = 2$.

The model was also utilized to assess the effects of grain length and burning rate exponent on BARF predictions. Results indicate that end surface contributions become unimportant at a grain L/D greater than two such that all longer grains had similar BARF behavior.[10] In addition, increasing burning rate exponent had essentially no effect on the BARF curve for fixed grain geometry and k values since the BARF effect is the burning rate amplification required to match the observed pressure history.

Conclusions

Results for a simple cylindrical-port motor indicate that inclusion of spatial dependence of burning rate produces effects similar in nature (both qualitatively and quantitatively) to those normally attributed to the BARF. These results indicate that future ballistic predictions could be improved if such a spatially-varying burning rate model were incorporated within the predictions. Spatial variations along axial-facing propellant surfaces are of minor importance for grain $L/D > 2$, and burning rate exponent has no influence on the level of the BARF effect for fixed grain geometry and spatial burning rate variations.

References

[1]Bradfield, W. A., "Some Observations on the Effect of Viscosity During Casting on the Burning Rate Uniformity in the Web of the Cast Composite Propellant Charge," Australian Weapons Systems Research Lab., WSRL-0163-TM, Salisbury, Australia, June 1980.

[2]Miles, W. L., Christensen, W. N., and Gill, M., "Directional Burn Rate Bias in Large Diameter Motors," 1990 JANNAF Combustion Meeting, Cheyenne, WY, Oct. 1990.

[3]Koury, J. L., "Solid Strand Burn Rate Technique for Predicting Fullscale Motor Performance," Air Force Rocket Propulsion Lab.-TR-73-49, Oct. 1973.

[4]Stark, J. A., and Taylor, R. E., "Determination of Thermal Transport Properties in Ammonium Perchlorate," *Journal of Propulsion and Power*, Vol. 1, No. 5, 1985, pp. 409, 410.

[5]Beckman, C. W., and Geisler, R. L., "Ballistic Anomaly Trends in Subscale Solid Rocket Motors," 18th AIAA/ASME Joint Propulsion Conf., AIAA Paper 82-1092, Cleveland, OH, 1982.

[6]Neilson, A. R., and Miles, W. L., "Space Shuttle Solid Rocket Motor Reproducibility and the Apparent Influence of Propellant Processing Characteristics on Trace Shape," 25th Joint Propulsion Conf., AIAA Paper 89-2310, Monterey, CA, 1989.

[7]Kallmeyer, T. E., and Sayer, L. H., "Differences Between Actual and Predicted Pressure-Time Histories of Solid Rocket Motors," 18th AIAA/ASME Joint Propulsion Conf., AIAA Paper 82-1094, Cleveland, OH, 1982.

[8]Lee, H. S., Misterek, D. L., Davis, R. J., and Fukuda, M. K., "Asymmetric Sidewall Insulation Erosion for Titan 34D and Titan IV Solid Rocket Motors," 25th AIAA/ASME/SAE/ASEE Joint Propulsion Conf., AIAA Paper 89-2772, Monterey, CA, 1989.

[9]Veit, P. W., Landuk, L. G., and Svob, G. J., "Experimental Evaluation of As-Processed Propellant Grains," *Journal of Propulsion and Power*, Vol. 1, No. 6, 1985, pp. 494–497.

[10]Heister, S. D., "Influence of Propellant Rheology on Ballistic Response of Solid Rocket Motors," 27th AIAA/SAE/ASME Joint Propulsion Conf., AIAA Paper 91-3394, Sacramento, CA, 1991.

Modeling of Spray Droplets Deformation and Breakup

E. A. Ibrahim*
Tuskegee University, Tuskegee, Alabama 36088
and
H. Q. Yang† and A. J. Przekwas‡
CFD Research Corporation, Huntsville, Alabama 35805

Introduction

ONE of the most important processes that dominate spray combustion efficiency is spray drop deformation and

Received Sept. 8, 1992; revision received March 1, 1993; accepted for publication March 8, 1993.

*Assistant Professor, Mechanical Engineering Department. Member AIAA.

†Project Engineer. Member AIAA.

‡Vice President. Member AIAA.

breakup. Krzeczkowski[1] has conducted an experimental study of the deformation mechanisms of spray drops. These may be characterized as bag-type and shear-type, with some transition in between. The present work is only concerned with the shear-type mechanism. Existing theoretical models for shear-type breakup may be categorized under two main categories. These are the 1) semianalytical and 2) the Taylor analogy models.

Semianalytical Models

The semianalytical models rely on analytical methods to solve the governing Navier-Stokes equations and mass conservation equation, with the aid of some submodels and assumptions. One of the most recent of these models is that of Gonor and Zolotova.[2] The original paper of Gonor and Zolotova[2] doesn't give the final equations and contains some misprints. The present authors worked out the equations for the axial and radial velocity components u and v, respectively, of the model of Gonor and Zolotova[2] to be

$$u = a_{00} + a_{10}x + a_{20}(x^2 - \tfrac{1}{2}y^2) + a_{40}(x^4 + \tfrac{3}{8}y^4 - \tfrac{3}{2}x^2y^2)$$

$$v = -\tfrac{1}{2}a_{10}y - a_{20}xy + a_{40}(\tfrac{3}{2}y^2 - 2x^2)xy$$

$$a_{00} = -(0.74/K)[(1 + lt)^{-2} - 1]$$

$$a_{10} = -(3/4K\omega)\sin(\omega t) + (3l/2K\omega^2)[1 - \cos(\omega t) - 3lt + (3l/\omega)\sin(\omega t)]$$

$$a_{20} = (5l/80K\omega_1)\sin(\omega_1 t) + (51l/40K\omega_1^2)[1 - \cos(\omega_1 t) - 3lt + (3l/\omega_1)\sin(\omega_1 t)]$$

$$a_{40} = -(5/28K\omega_2)\sin(\omega_2 t) + (5l/14K\omega_2^2)[1 - \cos(\omega_2 t) - 3lt + (3l/\omega_2)\sin(\omega_2 t)]$$

$$l = (9/8K), \qquad \omega = \sqrt{(8/KWe)}, \qquad \omega_1 = \sqrt{(30/KWe)}$$

$$\omega_2 = \sqrt{(140/KWe)}$$

with $lt << 1$ where x and y are the axial and radial coordinates, respectively; t is time, K is the liquid to gas density ratio, $K = \rho_l/\rho_g$, and We is the Weber number $We = \rho_g U_\infty^2 R/\sigma$, where U_∞ is the relative gas to liquid velocity, R is the spherical drop radius, and σ is surface tension. The axial and radial deformations of the drop are evaluated from the corresponding velocity components as

$$x_f = x_i + \int_{t_i}^{t_f} u \, dt$$

$$y_f = y_i + \int_{t_i}^{t_f} v \, dt$$

where subscripts i and f denote initial and final quantities, respectively. Unfortunately, the model of Gonor and Zolotova[2] gradually loses its time-accurate representation of the drop deformation as this deformation becomes large. Consequently, their power-series solution often diverges long before drop breakup occurs, especially at $We > 20$, as will be shown later. Also, Gonor and Zolotova neglected the viscosity of the drops which can be significant in predicting the oscillations of small drops.

Taylor Analogy Models

Taylor[3] suggested the analogy between an oscillating and distorting droplet and a spring-mass system. The restoring force of the spring is analogous to the surface tension forces. The external force on the mass is analogous to the gas aerodynamic force. The recent models based on the Taylor analogy have added the damping forces due to liquid viscosity. The equation of a damped, forced harmonic oscillator is given by

$$m\frac{d^2y}{dt^2} + c\frac{dy}{dt} + ky = F \tag{1}$$

The Taylor analogy models can be categorized by the approach that is used to determine the values of m, c, k, and F in Eq. (1). Two types of models exist: 1) models which use an empirical approach such as the Taylor analogy breakup (TAB) model of O'Rourke and Amsden,[4] and 2) others which employ an approximate analytical approach.[5] The equation of the TAB model can be written as

$$K\frac{d^2y}{dt^2} + \frac{5N}{Re}\frac{dy}{dt} + \frac{8}{We}y = \frac{2}{3} \tag{2}$$

where N is the liquid-to-gas dynamic viscosity ratio $N = \mu_l/\mu_g$, and Re is the Reynolds number $Re = U_\infty R/\nu_g$, where ν_g is the gas kinematic viscosity. In Eq. (2), y is the dimensionless displacement of the equator of the droplet from its equilibrium position. This is odd, because in a spring-mass system, the forces are expected to act through the c.m., and since the droplet deformation takes place at both its north and south poles simultaneously, the acting forces should be divided equally between the north and south halves of the droplet and act through the c.m. of the half droplet at distances $\pm 4R/(3\pi)$ from the equator. Then y in Eq. (2) should be the displacement of the c.m. of the half droplet. The displacement of the equator of the droplet vanishes symmetrically. The above-mentioned shortcoming of the TAB model was corrected in the drop oscillation model of Clark.[5] However, since Clark's model is linearized, the nonlinear effects which manifest themselves at large deformations of the drops are lost. The model preserves the cross-sectional area of the drops instead of its volume. The equation derived in this model is

$$(K + 1)\frac{d^2y}{dt^2} + \frac{9\pi^2(N + 1)}{4Re}\frac{dy}{dt} + \frac{9\pi^2}{4We}\left(y - \frac{4}{3\pi}\right) = \frac{2}{\pi} \tag{3}$$

where y is the dimensionless distance between the center of the deformed half-drop and the equator of the drop.

Proposed Model

It is assumed that the liquid drop is deformed due to a pure extensional flow from an initial spherical shape of radius R into an oblate spheroid of an ellipsoidal cross section with major semiaxis a and minor semiaxis b. We formulate the drop dynamics in terms of the motion of the c.m. of the half-drop. The energy equation of the half-drop that experiences no heat exchange with its surroundings can be written as

$$\frac{dE}{dt} = -\frac{dW}{dt} \tag{4}$$

where E is internal energy and W is work done. The internal energy of the half-drop comes from its kinetic and potential energies

$$\frac{dE}{dt} = \frac{2}{3}\pi R^3 \rho_l v\left(\frac{dv}{dt}\right) + \frac{1}{2}\sigma\frac{dA_s}{dt} \tag{5}$$

Here $v = (dy/dt)$, where y is the distance from the c.m. of the deforming half-drop to its equator, and A_s is the drop

surface area. The work done is by pressure and viscous forces, so that

$$\frac{dW}{dt} = -\frac{1}{2} pA_p \left(\frac{dy}{dt}\right) + \Phi \tag{6}$$

where p is pressure, A_p is the projected area of the drop $A_p \approx \pi R^2$, and Φ is the viscous dissipation. The pressure term in Eq. (6) contains (dy/dt), since all forces are assumed to act through the c.m. of the half-drop. Using the principal axis form of the two-dimensional strain-rate tensor, the viscous dissipation due to pure extensional flow is

$$\Phi = \frac{8}{3} \pi R^3 \mu_l \left(\frac{\partial v}{\partial z}\right)^2$$

where z is the principal axis which is in the direction of the motion of the c.m. of the half-drop. For an elliptic half-drop, the velocity of the c.m. in the z direction is $v = (\partial v/\partial z)y$, and with $v = (dy/dt)$ we get $(\partial v/\partial z) = (v/y) = (1/y)\,(dy/dt)$. Therefore, the viscous dissipation for the half-drop is

$$\Phi = \frac{8}{3} \pi R^3 \mu_l \left(\frac{1}{y}\frac{dy}{dt}\right)^2 \tag{7}$$

The pressure causing the drop deformation is the gas stagnant pressure, $\frac{1}{2}(\rho_g U_\infty^2)$. The average pressure on the drop front is actually less than the stagnation pressure, but this is partly counteracted by the negative pressure behind the drop. Hence

$$\frac{1}{2} pA_p \left(\frac{dy}{dt}\right) = \frac{\pi}{4} R^2 \rho_g U_\infty^2 \left(\frac{dy}{dt}\right) \tag{8}$$

For the ellipsoidal drop, the surface area is that of an oblate spheroid given by

$$A_s = 2\pi a^2 + \pi \frac{b^2}{\varepsilon} \ln \frac{(1+\varepsilon)}{(1-\varepsilon)}, \qquad \varepsilon = \sqrt{1 - \left(\frac{b}{a}\right)^2}$$

However, use of the above formula results in a somewhat complicated form of the model. In order to simplify the analysis, the above formula is approximated by

$$A_s = 2\pi(a^2 + b^2) \tag{9}$$

Equation (9) is found to give a good approximation of the surface area of the ellipsoidal drop within the deformation range considered in the present investigation. Since the drop volume is conserved, i.e., $\frac{4}{3}\pi a^2 b = \frac{4}{3}\pi R^3$, or $b = R^3/a^2$. Using $a = (3\pi/4)y$ and $b = R^3/a^2$ in Eq. (9), and putting $3\pi/4 = c$, we may write

$$\frac{dA_s}{dt} = \frac{9\pi^3}{4} y \left[1 - 2\left(\frac{cy}{R}\right)^{-6}\right] \frac{dy}{dt} \tag{10}$$

Using Eqs. (5), (6), (7), (8), and (10) in Eq. (4) gives

$$\frac{2}{3}\pi R^3 \rho_l \left(\frac{dy}{dt}\right)\left(\frac{d^2y}{dt^2}\right) + \frac{1}{2}\sigma \frac{9\pi^3}{4} y \left[1 - 2\left(\frac{cy}{R}\right)^{-6}\right]\left(\frac{dy}{dt}\right) + \frac{8}{3}\pi R^3 \mu_l \left(\frac{1}{y}\frac{dy}{dt}\right)^2 = \frac{1}{4}\pi R^2 \rho_g U_\infty^2 \left(\frac{dy}{dt}\right) \tag{11}$$

Defining the dimensionless quantities, $y^* = y/R$, $t^* = t(U_\infty/R)$, we can rewrite Eq. (11) in terms of these dimensionless quantities which yields after dropping the star

$$K\frac{d^2y}{dt^2} + \frac{4N}{Re}\frac{1}{y^2}\frac{dy}{dt} + \frac{27\pi^2}{16We} y[1 - 2(cy)^{-6}] = \frac{3}{8} \tag{12}$$

We call Eq. (12) the droplet deformation and breakup (DDB) model. The DDB model is applicable to shear-type (typically at $We > 20$) deformation of spray droplets in pure extensional flows.

Results and Discussion

A numerical solution of the DDB model equation is obtained by a fourth-order Runge-Kutta initial-value solver. The initial conditions are given by $y = dy/dt = 0$, at $t = 0$ for the TAB model and $y = 4/(3\pi)$, $dy/dt = 0$, at $t = 0$ for both Clark's[5] and the DDB models.

The predictions of the above three models, as well as the semianalytical model of Gonor and Zolotova,[2] are compared with the experimental data of Krzeczkowski[1] for shear breakup in Fig. 1 which depicts the dimensionless deformation of the drop vs dimensionless time. The dimensionless deformation of the drop is represented by the ratio of the deformed drop major semiaxis a to the initial undeformed drop radius R. In Gonor and Zolotova's[2] model, the deformation is given by the maximum value of y. In the TAB model it is equal to $(y + 1)$, while in Clark's[5] and the DDB models it is given by $a/R = (3\pi/4)y$. In Fig. 1 it is seen that calculations by the model of Gonor and Zolotova could only be carried out up to a short period of time, after which the model predicts an infinite drop deformation. It is clear from Fig. 1 that the DDB model provides a better agreement with the experimental data compared with the TAB and Clark models. The cross on the curves of the TAB and DDB models represents predictions of drop breakup time for shear breakup. In the TAB model, the breakup criterion is that the amplitude of oscillations of the north and south poles of the drop equals the drop radius. This is believed to be rather unrealistic since experimental evidence, e.g., Krzeczkowski,[1] suggests that breakup occurs at different drop sizes for different We numbers. The breakup criterion in the present DDB model is derived by noting that near drop breakup, both the drop kinetic energy and viscous dissipation are negligible.[4,5] Therefore, from Eq. (12) we have

$$\left(\frac{a}{R}\right)_b = \frac{3\pi}{4} y_b \approx \frac{3\pi}{4}\frac{3}{8}\frac{16We}{27\pi} = \frac{We}{6\pi} \tag{13}$$

where subscript b denotes breakup quantities. The agreement between Eq. (13) and the experimental data is favorable as shown in Fig. 1.

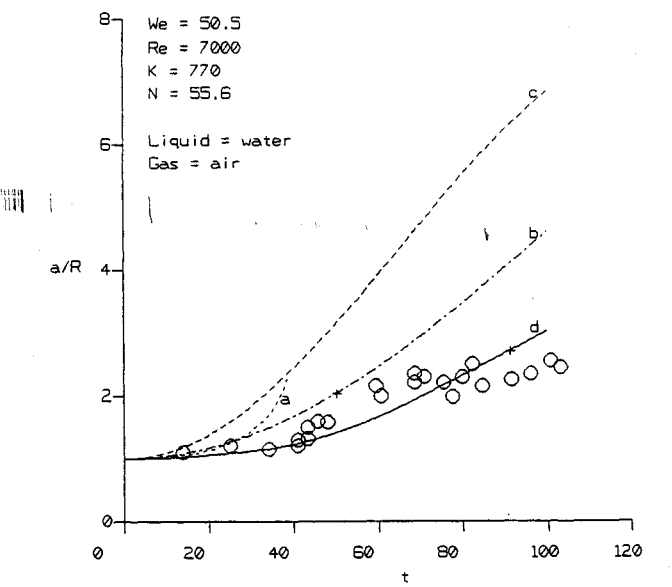

Fig. 1 Comparison of predicted drop deformation and breakup with the experimental data of Krzeczkowski.[1] ○ (Ref. 1), a (Ref. 2), b (Ref. 4), c (Ref. 5), d (DDB).

Acknowledgment

This work was supported by NASA MSFC Grant NAS8-38425.

References

[1]Krzeczkowski, S. A., "Measurement of Liquid Droplet Disintegration Mechanisms," *International Journal of Multiphase Flow*, Vol. 6, No. 1, 1980, pp. 227–239.

[2]Gonor, A. L., and Zolotova, N. V., "Spreading and Breakup of a Drop in a Gas Stream," *Acta Astronautica*, Vol. II, No. 2, 1984, pp. 137–142.

[3]Taylor, G. I., "The Shape and Acceleration of a Drop in a High Speed Air Stream," *The Scientific Papers of G. I. Taylor*, edited by G. K. Batchelor, Vol. III, Univ. Press, Cambridge, UK, 1963.

[4]O'Rourke, P. J., and Amsden, A. A., "The Tab Method for Numerical Calculation of Spray Droplet Breakup," Society of Automotive Engineers Paper 87-2089, 1987.

[5]Clark, M. M., "Drop Breakup in a Turbulent Flow-I, Conceptual and Modeling Considerations," *Chemical Engineering Science*, Vol. 43, No. 3, 1988, pp. 671–679.

Liftoff Characteristics of Methane Jet Diffusion Flames

J. P. Seaba* and L.-D. Chen†
University of Iowa, Iowa City, Iowa 52242
and
W. M. Roquemore‡
Wright Laboratory,
Wright-Patterson Air Force Base, Ohio 45433

Nomenclature

d = inner diameter of burner exit
R = inside radius of burner exit
r = radial position from center of burner exit
Uc = average centerline velocity
Um = average axial velocity
$Urms$ = root mean square velocity
X_i = mole fraction of fuel with inert gas i
x = position normal to burner exit

Introduction

THE mechanisms responsible for the liftoff from the burner rim and stabilization of jet flames are not clearly understood.[1] Early works[2,3] studied the stability of jet flames in open air and identified four different regimes concerning flame stability. Of the four stability regimes 1) liftoff, 2) blowoff, 3) lifted, and 4) blowout, only the liftoff process will be studied in this Note. The liftoff condition is referred to the instant when the flame detaches from the burner rim in a discontinuous manner. After the flame detaches from the burner rim, it may stabilize at a downstream location (i.e., lifted flame) or it may result in flameoff conditions (or the blowoff condition).

Received July 13, 1991; revision received Feb. 25, 1993; accepted for publication Feb. 28, 1993.

*Graduate Reearch Assistant, Department of Mechanical Engineering; currently Assistant Professor, Department of Mechanical and Aerospace Engineering, University of Missouri—Columbia, Columbia, MO 65211. Member AIAA.

†Professor, Department of Mechanical Engineering. Member AIAA.

‡Aero Propulsion and Power Directorate. Member AIAA.

More recent works[4–7] have determined important parameters such as jet exit lip thickness, annular velocity, diluents, etc., which significantly effect the liftoff process. Current data are inconclusive to determine the mechanism(s) responsible for the liftoff process. The present study adds new information to the data base and reveals interesting comparisons to previous liftoff data.

Experimental Consideration

The experiments were conducted with a small vertical combustion tunnel.[8] The fuel and inert gas flows are regulated by rotameters. The burner is positioned vertically upward, at the center of the coflowing annular air that has a diameter of 250 mm. The burner tip extends 25-mm above the annulus exit plane. A stainless steel honeycomb mesh is placed in the annulus perpendicular to the axial direction, upstream of the burner exit. The burner assembly is situated under a forced-draft exhaust hood (1.22 × 1.22 m) with window screens surrounding the combustor. The exhaust system is equipped with a blower rated at 0.944 m³/s. The dry annulus air (dew point at −40°C) is metered by a mass flow meter. The inert gas is added only to the fuel flow. A pressure gauge downstream of the rotameters is used to monitor the pressure drop between the rotameters and the burner exit. The pressure drop for the conditions reported here is less than 0.69 kPa, which has a negligible back-pressure effect relative to the rotameter reading. The flow meters are specified with an accuracy of ±5% of the full-scale reading. Liftoff conditions were recorded with and without the exhaust hood operating; no difference in the liftoff velocities was observed.

The burner configuration is a tapered nozzle. The burner exit i.d. is 5 mm. The burner is made of a long stainless steel tube, having an o.d. of 25.4 mm, and a reducing section near the burner tip. The tapered nozzle has a gradually tapered section, at a rate of 1–20 radius-to-length ratio, over a length of 100 mm, forming a 2.9-deg angle to the vertical plane. The tapered burner has a sharp lip, about 0.3 mm in thickness, and yields a flat velocity profile at the burner exit as shown in Fig. 1.

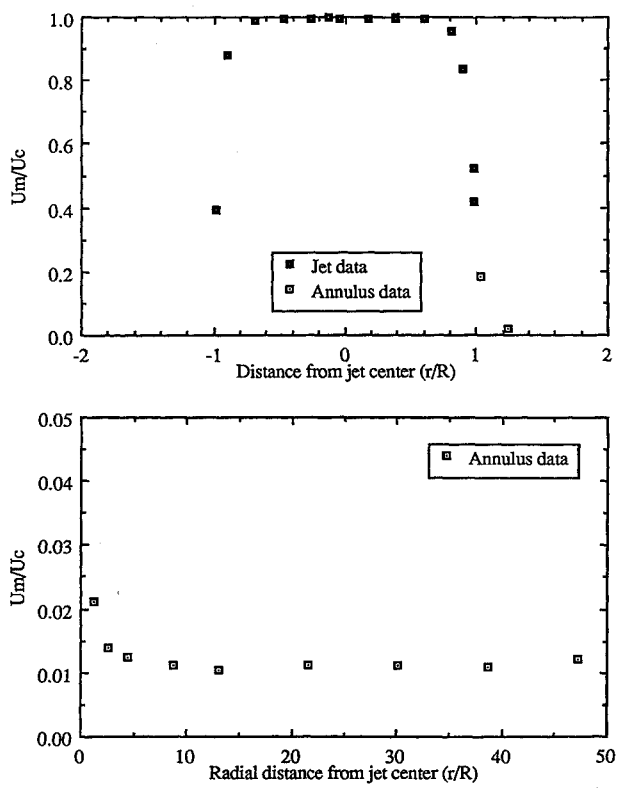

Fig. 1 Average velocity profile using argon jet at condition B, x/d = 0.4.